



Published in final edited form as:

Appl Surf Sci. 2012 November 15; 261: . doi:10.1016/j.apsusc.2012.09.013.

Solid-State Densification of Spun-Cast Self-Assembled Monolayers for Use in Ultra-Thin Hybrid Dielectrics

Daniel O. Hutchins¹, Orb Acton¹, Tobias Weidner², Nathan Cernetic¹, Joe E. Baio³, David G. Castner^{2,3}, Hong Ma^{1,a}, and Alex K.-Y. Jen^{1,4,a}

¹Department of Materials Science and Engineering, University of Washington, Seattle, Washington 98195

²Department of Bioengineering, University of Washington, Seattle, Washington 98195

³Department of Chemical Engineering, University of Washington, Seattle, Washington 98195

⁴Department of Chemistry, University of Washington, Seattle, Washington 98195

Abstract

Ultra-thin self-assembled monolayer (SAM)-oxide hybrid dielectrics have gained significant interest for their application in low-voltage organic thin film transistors (OTFTs). A [8-(11-phenoxy-undecyloxy)-octyl]phosphonic acid (PhO-19-PA) SAM on ultrathin AlO_x (2.5 nm) has been developed to significantly enhance the dielectric performance of inorganic oxides through reduction of leakage current while maintaining similar capacitance to the underlying oxide structure. Rapid processing of this SAM in ambient conditions is achieved by spin coating, however, as-cast monolayer density is not sufficient for dielectric applications. Thermal annealing of a bulk spun-cast PhO-19-PA molecular film is explored as a mechanism for SAM densification. SAM density, or surface coverage, and order are examined as a function of annealing temperature. These SAM characteristics are probed through atomic force microscopy (AFM), X-ray photoelectron spectroscopy (XPS), and near edge X-ray absorption fine structure spectroscopy (NEXAFS). It is found that at temperatures sufficient to melt the as-cast bulk molecular film, SAM densification is achieved; leading to a rapid processing technique for high performance SAM-oxide hybrid dielectric systems utilizing a single wet processing step. To demonstrate low-voltage devices based on this hybrid dielectric (with leakage current density of 7.7×10^{-8} A cm⁻² and capacitance density of 0.62 μF cm⁻² at 3 V), pentacene thin-film transistors (OTFTs) are fabricated and yield sub 2 V operation and charge carrier mobilities of up to 1.1 cm² V⁻¹ s⁻¹.

Keywords

Self Assembled Monolayer (SAM); SAM Dielectric; Hybrid Dielectric; SAM Processing; Organic Field Effect Transistor (OFET); Organic Thin Film Transistor (OTFT)

1. Introduction

Organic thin-film transistors (OTFTs) have become a field of interest due to their application in low-cost, flexible, solution processed electronic devices [1–4]. Potential uses include but are not limited to radio-frequency identification (RFID) tags, electronic paper, chemical sensors, and background circuitry to active matrix displays [5–8]. Although much work in the OTFT field has been aimed at increasing device performance by improving the

^ahma@uw.edu, ajen@uw.edu.

semiconducting layer through tuning molecular design and/or processing of small-molecule/polymeric materials that it is comprised of, it has been demonstrated that modification of the gate dielectric can be equally influential [9–13].

Manipulation of the dielectric layer has been accomplished both through organic and inorganic means, however, recently hybrid inorganic/organic ultra-thin dielectric materials have attracted attention for their robust insulating properties and ease of processing [14–16]. One method of obtaining these hybrid structures is through merging inorganic oxides and self-assembled monolayers (SAMs) [17]. This technique has been demonstrated by several groups and has proven to be quite successful, allowing the formation of sufficiently insulative layers that are less than 10 nm in thickness [18–20]. Through molecular design, electronic properties of these structures can be tailored to meet the needs of a wide variety of device constraints [13,21,22]. However, several obstacles have yet to be overcome in order to make this approach to forming OTFT dielectrics ubiquitous.

One such limiting factor in the creation of an ideal inorganic oxide/SAM hybrid dielectric is the binding chemistry employed to anchor SAM molecules to the substrate surface. Anchoring has been achieved through a variety of chemical processes, however, many techniques possess drawbacks that make their implementation highly situational. Several methods of adhesion commonly found in self-assembly literature and employed for hybrid dielectric enhancement are as follows: Molecular physisorption to a substrate surface has been demonstrated to be a viable means of self-assembly for dielectric formation. However, as these molecules are not chemically bound to the substrate, their resilience to mechanical forces proves to be problematic [23]. Alternatively, silane based chemistry allows for direct chemical anchoring to a wide range of inorganic oxides and has several different binding moieties ($\text{Si}(\text{Cl})_{1-3}$, or $\text{Si}(\text{OR})_{1-3}$). Unfortunately, high reactivity results in several undesirable traits such as a propensity for homocondensation, sensitivity to moisture, and potential for aggregate formation on substrate surfaces if reaction conditions are not precisely controlled [24–26]. Conversely, carboxylic acids exhibit reduced reactivity with oxide surfaces, however, this can prove to be equally problematic in achieving dense, high coverage assemblies [27–33]. Due to the drawbacks associated with silane/carboxylic acid chemistry, phosphonic acids (PAs) have become an attractive alternative for their reactivity with a wide range of metal oxides, ambient stability, and inability to homocondense [10, 34–36].

Dense and ordered PA self-assembly is typically accomplished by lengthy immersion time in dilute solutions, sometimes in excess of 16 hours [34a]. Well-packed SAM structures have been achieved by rapid spin coating processes and microcontact printing [34b, 37a]. However, papers describing self-assembly by spin casting/printing often only achieve this with simple alkyl-structures that do not provide steric hindrance sufficient to block other SAM molecules from reaching the substrate surface and/or do not provide significant characterization of the monolayer. In this manuscript, chemically complex aryl-alkyl-PA SAMs are formed by spin coating a molecular multilayer. Through thermal annealing of the bulk film, rather than subsequent wet processes, rapid densification is achieved, conserving solvent, compound, and time. Characterization of this processing technique is examined through various spectroscopic methods and proven to facilitate the spin casting of SAMs with complex molecular structures that exhibit non-negligible steric effects during self-assembly and normally do not achieve dense packing.

It should be noted that the solid state densification procedure presented here is generally applicable to large SAM molecular structures besides PhO-19-PA that do not normally form highly ordered monolayers through rapid immersion [36b]. However, in this manuscript PhO-19-PA will be exclusively used to systematically characterize this processing technique

and demonstrate its applicability in forming high performance hybrid SAM-metal oxide dielectrics.

2. Materials and Methods

2.1 PhO-19-PA Synthesis

The PhO-19-PA,[8-(11-phenoxy-undecyloxy)-octyl]phosphonic acid, molecule was synthesized through the following procedures (Scheme 1).

All chemicals were purchased from Aldrich and used as received unless otherwise specified. Tetrahydrofuran (THF) was distilled under nitrogen from sodium with benzophenone as the indicator. Methylene chloride was distilled over P₂O₅ and 11-Phenoxy-1-undecanol (**1a**) was synthesized following the reported method [37b]. ¹H NMR spectra (300 MHz) were taken on a Bruker-300 FT NMR spectrometer with tetramethylsilane (TMS) as internal reference. Elemental analysis was determined at QTI (Whitehouse, NJ). ESI-MS spectra were obtained on a Bruker Daltonics Esquire Ion Trap Mass Spectrometer.

11-(8-Bromooctoxy)undecyloxybenzene (1b)—To a mixture of 1,8-dibromooctane (3.26 g, 12.0 mmol) and sodium hydride (0.384 g, 16.0 mmol) in dry THF (30 mL) under nitrogen was dropwise added the solution of 11-phenoxy-1-undecanol (**1a**) (1.06 g, 4.0 mmol) in dry THF (5 mL). The mixture was stirred overnight under reflux, cooled down to room temperature and filtered to remove insoluble salts. The filtrate was concentrated by rotary evaporation under reduced pressure. The crude product was purified over silica gel column chromatography with hexane:methylene chloride (3:1) as the eluent to afford a white solid (1.43 g, 79%). ¹H NMR (300 MHz, CDCl₃): 7.27–7.33 (m, 2H), 6.89–6.98 (m, 3H), 3.97 (t, 2H, *J* = 6.6 Hz), 3.38–3.45 (m, 6H), 1.25–1.91 (m, 30H). C₂₅H₄₃BrO₂: Calcd C 65.92, H 9.51, Br 17.54; Found C 66.07, H 9.58, Br 17.46. ESI-MS (*m/z*): Calcd. 454.2; Found 454.1.

Diethyl 8-(11-phenoxy)undecyloxyoctylphosphonate (1c)—A mixture of **1b** (0.91 g, 2.0 mmol) and triethyl phosphite (9.55 g, 10.0 mL) was heated under nitrogen at 150 °C for 20 h. The excess of triethyl phosphite was removed by distillation under vacuum. The crude product was purified over silica gel column chromatography with methylene chloride to methylene chloride:ethyl acetate (5:1) as the eluents to afford a white solid (0.72 g, 70%). ¹H NMR (300 MHz, CDCl₃): 7.23–7.31 (m, 2H), 6.87–6.90 (m, 3H), 4.04–4.12 (m, 4H), 3.95 (t, 2H, *J* = 6.6 Hz), 3.35–3.42 (m, 4H), 1.28–1.81 (m, 38H). C₂₉H₅₃O₅P: Calcd C 67.94, H 10.42, P 6.04; Found C 68.05, H 10.51, P 5.95. ESI-MS (*m/z*): Calcd. 512.4; Found 512.4.

8-(11-Phenoxy)undecyloxyoctylphosphonic acid (1)—To a solution of **1c** (0.385 g, 0.75 mmol) in dry methylene chloride (20 mL) under nitrogen was dropwise added bromotrimethylsilane (0.689 g, 0.58 mL, 4.50 mmol). The mixture was stirred overnight at room temperature. The reaction mixture was poured into water (200 mL), filtered and washed with large amount of water to collect a white solid (0.272 g, 80%). ¹H NMR (300 MHz, CDCl₃): 7.50–7.95 (s, br, 2H), 7.23–7.30 (m, 2H), 6.80–6.95 (m, 3H), 3.95 (t, 2H, *J* = 6.6 Hz), 3.35–3.42 (m, 4H), 1.10–1.80 (m, 32H). C₂₅H₄₅O₅P: Calcd C 65.76, H 9.93, P 6.78; Found C 65.87, H 10.02, P 6.71. ESI-MS (*m/z*): Calcd. 456.3; Found 456.3.

2.2 Substrate Preparation

Heavily P-doped (boron, 0.01–0.02 ohm-cm) native oxide silicon substrates were cleaned by piranha etching H₂SO₄:H₂O₂ (volume ratio, 3:1) for 10 minutes, followed by immersion in H₂O:H₂O₂:NH₄OH (5:1:1) at 80 °C and through rinsing in DI H₂O. If these experimental

conditions are reproduced, care should be taken to avoid accidental exposure to any etchant solutions as they are extremely caustic.

2.3 Dielectric Fabrication

Clean substrates were placed in a Diener Femto low-pressure air plasma system for 10 minutes directly beneath an overhanging aluminum electrode operating at 40 kHz. This has been shown by our group to deposit a ~2.5nm thick layer of AlO_x on substrate surfaces as previously verified by time of flight secondary ion mass spectroscopy (TOF-SIMS) [17]. The PhO-19-PA SAM was prepared on the Si native oxide/AlO_x layer via spin coating from a 3 mM solution in chloroform: tetrahydrofuran (THF) (4:1) at 3k RPM for 30 seconds. The bulk SAM coated substrate was then subject to the appropriate annealing/cleaning conditions used to explore mechanisms of SAM formation. The condition deemed ideal for the assembly of a well ordered SAM with excellent dielectric properties is as follows: post spin coating, the multilayer-covered substrates were subjected to annealing at 140 °C for 10 minutes followed by the rinse-off of bulk molecular aggregate. This rinsing process consisted of sonication in triethylamine: dimethylformamide (1:20) for 10 minutes followed by a five-minute sonication in THF and a five-minute sonication in ethanol. Annealing temperatures above 140 °C were explored, however, no further SAM densification was observed and substrate surface morphology worsened, therefore, these experiments will not be discussed in further detail.

The same dielectric architecture using n-octadecylphosphonic acid (99.9% purity PCI Synthesis) in lieu of PhO-19-PA was fabricated to provide a comparison between the two molecules. Substrates were cleaned and plasma treated in an identical manner. ODP was spun cast from a 1:4 THF:chloroform solution, annealed at 140 °C for 10 minutes, and cleaned via sonication in THF then hexanes.

2.4 SAM Characterization: Atomic Force Microscopy

Images were taken in tapping mode using a Multimode Nanoscope III atomic force microscope made by Digital Instruments. Etched silicon tips were used with resonant frequencies between 300 and 350 kHz. Roughness measurements were calculated using NanoScope Analysis V1.20 from scan sizes of 2 μm by 2μm.

2.5 SAM Characterization: Near-Edge X-ray Absorption Fine Structure Spectroscopy (NEXAFS)

Spectra were measured at the National Synchrotron Light Source (NSLS) U7A beamline at Brookhaven National Laboratory, using an elliptically polarised beam with ~85% *p*-polarisation. A monochromator with 600 l/mm grating provided a full-width at half-maximum (FWHM) resolution of ~0.15 eV at the carbon *K*-edge (285 eV). The monochromator was calibrated using the 285.35 eV C 1s * transition on a graphite transmission grid placed in the upstream path of the X-rays. C *K*-edge spectra were normalized by the spectrum of a clean gold surface prepared by evaporation of gold in vacuum. Both reference and sample signals were divided by the NEXAFS signal of a gold-coated reference mesh to account for beam intensity variations.

2.6 SAM Characterization: X-Ray Photoelectron Spectroscopy (XPS)

The SAMs were characterized by XPS with a Kratos AXIS Ultra DLD instrument (Kratos, Manchester, England) in the hybrid mode using a monochromatic Al_K X-ray source (photon energy = 1486.6 eV) and normal emission geometry. The XPS determined compositions were an average from three spots on two replicates. Atomic compositions were calculated from peak areas obtained from 0 – 1100 eV survey scans (C 1s, Au 4f) and

selected region scans (O 1s, P 2s, Si 2p) acquired at an analyzer pass energy of 80 eV. A linear background was subtracted for all peak quantifications. The peak areas were normalized by the manufacturer-supplied sensitivity factors and surface concentrations were calculated using Casa XPS software.

2.7 Dielectric Characterization

Agilent 4284B LCR Meter was used for dielectric capacitance characterization. Thermally evaporated gold squares (area: 4×10^{-4} cm², evaporated at 1 Å/s, 50 nm final thickness) were used as the top electrodes and the electrically conductive heavily P-doped Si substrate was used as a universal bottom electrode.

2.8 OTFT Device Construction

Substrates with hybrid dielectrics fabricated in the aforementioned manner (see Dielectric Fabrication) were placed in a thermal evaporator and allowed to heat to 60 °C under high vacuum. Pentacene (99.95% Aldrich) was evaporated at 0.2 Å/s until the desired thickness of 40 nm was reached. Substrates were cooled to room temperature under high vacuum prior to the thermal evaporation of source and drain electrodes. Gold electrodes were patterned by shadow mask and evaporated at 1 Å/s for a final thickness of 50 nm.

2.9 OTFT Device Characterization

Transistor characterization was performed in a dry N₂ environment using Agilent 4155B semiconductor parameter analyser. Field effect mobility (μ) was calculated in the saturation regime using a linear fit of $(-I_{ds})^{1/2}$ vs. V_{gs} . Threshold voltage (V_t) was calculated as the x-intercept of the linear section of the $(I_{ds})^{1/2}$ versus V_{gs} plot. Subthreshold swing (S) was calculated by the inverse slope of I_{ds} versus V_{gs} in the region of exponential current increase.

3. Results and Discussion

3.1 Rationale of Molecular Design

The PhO-19-PA molecule (Fig. 1A) was designed as phenyl-terminated alkylphosphonic acid. It has been demonstrated that aliphatic chain length can substantially influence the ability of molecules to self-assemble in a manner favorable to the enhancement of dielectric properties. Longer chain lengths reduce leakage current and provide a greater barrier for electron tunnelling [21,38]. Conversely, short chain lengths do not provide enough enthalpic gain due to Van der Waals interactions to provide significant ordering effects. Phosphonic acid bound alkyl-chain lengths of 18 CH₂ or longer form highly ordered structures, thus PhO-19-PA was specifically designed to maximize this interaction [10,34]. Aromatic terminal structures are known to improve dielectric properties of SAMs by enhancing intermolecular interaction through π -stacking [39]. Through integration of the aforementioned molecular design principals, PhO-19-PA molecule attempts to maximize dielectric properties of its SAM while maintaining solubility in a wide range of solvents, making it compatible with the fabrication of many device architectures.

3.2 Oxide Structure and SAM Formation by Spin Coating

The oxide structure used in this study was made by a plasma-enhanced deposition of AlO_x onto the silicon native oxide surface of a highly P-doped wafer. From AFM images it can be seen that this surface has an almost identical morphological appearance to Si native oxide, with an RMS roughness of ~0.2 nm. Following AlO_x deposition, a 3 mM solution of PhO-19-PA is prepared in THF:chloroform (1:4) and spun cast onto the substrate at 3k RPM to form the remainder of the hybrid dielectric structure (Fig. 1B).

Spin coating of phosphonic acid monolayers has been previously investigated by H.-Y. Nie et al [40]. In their work, octadecylphosphonic acid (ODPA) was spun coat onto mica and other oxide surfaces from a 2 mM solution of nonpolar trichloroethane solvent. Post spin coating, substrates were examined under AFM and the portion of the surface covered by ODPA was determined by the ~2 nm variations in height seen between SAM and substrate. From this experiment it was determined that the first spin coating step from a relatively nonpolar solvent results in segregated island-like formations of ODPA on the surface of the substrate. However, subsequent spin coating experiments using more polar solvents resulted in much less dense SAM coverage. It was hypothesized that due to the polar nature of the phosphonic acid binding group and nonpolar nature of the aliphatic chain, organization of ODPA was occurring in solution. In nonpolar solvent, ODPA head groups are pushed towards the air-solvent interface while the tails remain solubilized, forming ordered rafts of phosphonic acid on the surface of the solvent. Upon spin casting, these organized molecular structures are transferred to the substrate when rafts of phosphonic acid head groups come in contact with the oxide surface.

Nie's hypothesis directly pertains to the PhO-19-PA SAM system and forms the basis for the initial SAM assembly step employed here. Islands of highly ordered SAMs bound to the AlO_x layer are formed on the substrate surface. Despite this, we believe significant defects are present in the SAM including regions of low density, voids, and molecular-misorientation (Fig. 2, step 1). As strong van der Waals forces and π - π interactions are present between PhO-19-PA molecules, a bulk multilayer is present on the surface of the substrate post spin coating. The presence of this multilayer prevents direct examination of bound monolayer by AFM. To examine the underlying SAM a thorough rinsing process in DMF:TEA (20:1), THF, and ethanol was employed. However, after cleaning, it is evident that initial spin coating has indeed resulted in island SAM formation. Post rinsing, boundaries between regions of formed monolayer are clearly present and characterized by dark surface discontinuities in AFM images (Fig. 3-1B).

After spin casting of the multilayer and rinsing, dielectric properties are less than ideal despite the formation of monolayer islands. Although Nie *et al.* found that densification of the SAM could be achieved through subsequent spin coating steps, this technique requires additional SAM compound, solvent, and time. As a means of reducing the impact of processing conditions, our group investigated the possibility of using the residual bulk PhO-19-PA on the surface of substrate as the source of material for additional SAM densification. Through the employment of proper annealing methods it was found that molecular multilayers could be used to sufficiently densify or improve the surface coverage of the SAM, resulting in a high quality ultra-thin dielectric, compatible with ambient solution processed device architectures and a single wet processing step. A cartoon representation of proposed mechanisms responsible for densification can be seen in Fig. 2.

3.3 AFM Characterization

From AFM images obtained of both the bulk molecular PhO-19-PA film present after spin coating (Fig. 3, column A), and underlying SAM made visible after solvent cleaning (Fig. 3, column B), dramatic changes in SAM morphology are seen with increased annealing temperatures. Following spin coating without annealing, a bulk molecular layer is clearly shown on the substrate surface (Fig. 3-1A), and upon its removal by solvent cleaning, a low-density, patchy SAM characterized by large dark grain boundaries on the AFM image is shown (Fig. 3-1B). Changes to the substrate surface morphology can be observed when the bulk film is thermally annealed. By heating for 10 minutes at 60 °C, the bulk layer begins to transform from a continuous film into a segregated structure (Fig. 3-3A). Additionally, voids in the underlying SAM begin to fill, resulting in a more densely packed monolayer (Fig. 3-3B). At 80 °C the bulk film has melted, forming large grains of residual material and the

underlying SAM lacks viable voids by AFM (Fig. 3-4A & 4B). For both 100 °C and 120 °C bulk material left on the surface has formed liquid-like droplets (Fig. 3-5A & 6A) and the SAM has the same appearance/similar roughness as bare Si (Fig. 3-5B & 6B) (0.2 nm RMS roughness), indicative of a densely packed monolayer. Although further densification occurs up to 140 °C, as shown by XPS and NEXAFS, AFM images of the SAM and bulk film at 140 °C look identical to those annealed at 120 °C and therefore are not shown in Fig. 3.

Based on the morphological transitions of the bulk PhO-19-PA molecular film seen at elevated temperature, we propose that SAM densification is occurring by liquefaction of the bulk compound facilitating molecular rearrangement (Fig. 2). Upon melting, molecules that did not penetrate into grain boundaries in the SAM during the initial spin coating step are allowed to reorient themselves in a manner that is favorable to surface binding. Through their increased molecular surface mobility due to thermal activation, surface spaces not previously occupied are filled.

The onset of melting for the bulk PhO-19-PA compound was determined through differential scanning calorimetry to occur at roughly 59 °C, with complete liquefaction at 89 °C. This is in good agreement with phase changes observed by AFM; further validating the hypothesis of increased SAM surface coverage through thermal activation.

3.4 XPS and NEXAFS Analysis

AFM observations are corroborated with X-ray photoelectron spectroscopy (XPS). The elemental composition of the hybrid SAM-oxide dielectric structures after spin-casting, annealing the bulk film at 25 °C, 60 °C, 100 °C, 140 °C for 10 min, and solvent cleaning, respectively, were determined by XPS. The surface composition, uncorrected for attenuation effects (Table 1), showed the presence of carbon, phosphorous, oxygen, and silicon (from the underlying substrate). The oxygen can be attributed to both, the SAM and the oxide substrate. The C/P ratio is an indicator of SAM order and this values increases slightly at the highest annealing temperatures [34]. The C/Si ratio describes the surface coverage and it shows surface carbon concentration increase with annealing temperature, in line with the observed densification by AFM (Fig. 3). After the initial spin coating the C/Si ratio is 3.5 and by annealing at 140 °C, an increase to 5.4 is achieved. Contrary to AFM images, this shows that the SAM density/surface coverage continues to increase at temperatures well above T_m of the bulk molecular layer up to 140 °C.

The chemical state and structure of the SAMs were also studied with NEXAFS spectroscopy. NEXAFS spectra provided insight into the electronic structure of surfaces by sampling unoccupied molecular orbitals [41]. Structural parameters like alignment, order and orientation in monomolecular films can be probed using the linear dichroism of X-ray absorption by recording the dependence of absorption resonance intensities on the orientation of the electric field vector of the synchrotron X-ray beam with respect to the orientation of molecular orbitals. The linear dichroism can be monitored by measuring spectra at normal and glancing X-ray incidence angles with respect to the sample surface. Spectra collected at 55°, the 'magic angle', are not affected by molecular orientation and are therefore only representative of the electronic and chemical state of the surface.

C K-edge spectra for SAMs with different annealing temperatures acquired at an X-ray incidence angle of 55° are presented in Fig. 4A. All spectra exhibit an absorption edge related to the excitation of the C 1s electrons into the continuum states and additional characteristic absorption resonances. The spectra show the π^* resonance of the terminal phenyl moiety near 285.6 eV. The spectra also exhibit a weak Rydberg resonance (R^*) near 287.6 eV mostly related to the aliphatic chains, and broad σ^* resonances related to C-C

bonds at higher photon energies [41–44]. The spectra are very similar and indicate intact SAMs with no indications of C=O or other chemical impurities [41, 45–47].

Fig. 4B displays the respective $70^\circ - 20^\circ$ difference spectra. The sample prepared at 25°C shows a weak negative dichroism for the R^* resonance, a signature of strongly inclined and mostly disordered chains. A difference peak for the phenyl moiety is not detected, indicating the phenyl groups are disordered. The 60°C sample shows no dichroism and the film is most likely disordered. The SAMs annealed at 100°C and 140°C , however, show pronounced linear dichroisms for both the chains and the phenyl groups. The polarity of the difference peaks indicates the phenyl group and the chain are oriented upright. The film annealed with 140°C shows the highest degree of order. We performed a more quantitative analysis of the molecular orientation using relative resonance intensities for the π^* and the R^* resonances based on published procedures [41,48]. The analysis yields tilt angles of $31^\circ \pm 5^\circ$ and $30^\circ \pm 5^\circ$ versus the surface normal for the alkyl chains and the phenyl rings, respectively. Similar values have also been observed for well-ordered aliphatic SAMs on gold and SiO_2 , while thiol SAMs on silver ($\approx 14^\circ$), platinum ($< 15^\circ$) and gallium arsenide ($\approx 18^\circ$) have shown more upright orientations [49–52].

3.5 Dielectric Characterization

To further evaluate the mechanism of densification and examine the effectiveness of the PhO-19-PA SAM-oxide structure as a dielectric, leakage current and breakdown voltage were evaluated (Fig. 5). To quantify the effect of the SAM, dielectric properties of the AlO_x/Si native oxide layer were first analyzed resulting in very high leakage currents (10^{-5} A cm^{-2}) at 3 V, and low breakdown voltages ($\sim 4\text{ V}$), making it unsuitable for a dielectric material. Upon initial application of the SAM, a one to two order of magnitude drop in 3-volt-leakage-current can be observed. After annealing the bulk film, large drops in leakage current are demonstrated. Most notably, at 140°C , leakage current reaches $7.7 \times 10^{-8}\text{ A cm}^{-2}$. Although reduction of leakage current several orders in magnitude is facilitated by the addition of the SAM to the underlying AlO_x/Si native oxide layer, capacitance with respect to applied voltage changes little with the presence of the monolayer, dropping from $0.96\ \mu\text{F cm}^{-2}$ to $0.62\ \mu\text{F cm}^{-2}$ at three volts.

For comparison, the same dielectric structure was fabricated with n-octadecylphosphonic acid (ODPA) instead of PhO-19-PA, and it exhibited leakage current on the order of 10^{-5} – 10^{-6} A cm^{-2} at 3 V. This further validates the importance of establishing a rapid processing procedure for molecularly complex SAMs, as the advantages conferred by such molecules in dielectric architectures are clearly shown by the 2–3 order of magnitude drop in leakage current between ODPA and PhO-19-PA monolayers.

3.6 Low-Voltage Pentacene OTFTs

To demonstrate the potential of this dielectric material in OTFTs, top-contact pentacene devices were fabricated. After construction of a hybrid dielectric using the ideal processing conditions, substrates were placed in a thermal evaporator and allowed to heat to 60°C to ensure optimal pentacene growth conditions. Segregated regions of pentacene were then evaporated onto the surface of the substrates at $0.2\ \text{\AA s}^{-1}$ using shadow mask. Once the evaporation was complete substrate were allowed to cool back to room temperature. Top contact gold electrodes were evaporated at $1\ \text{\AA s}^{-1}$ and patterned with shadow mask.

$20\ \mu\text{m}$ channel length pentacene devices were found to exhibit excellent low-voltage performance. For V_{ds} and $V_{\text{gs}} = 2\text{ V}$, charge carrier mobiles of up to $1.1\text{ cm}^2\text{ V}^{-1}\text{ s}^{-1}$ were observed (Fig. 6 & Table 2). Additionally, minimal hysteresis is shown to exist in both output and transfer curves.

4. Conclusion

Ultra-thin hybrid dielectric structures utilizing SAMs and inorganic oxides result in highly functional components of OTFT device architectures. Processing of molecularly complex SAMs capable of providing sufficient insulating properties can be achieved through rapid solid state annealing of spun cast bulk molecular films. This technique results in reduced solvent and compound requirements when compared with traditional wet processes. Solid state PhO-19-PA SAM densification was studied with AFM, XPS and NEXAFS. It was shown that PhO-19-PA SAM densification occurs rapidly at $T > T_m$ of the bulk film, with SAM density/order maximized at an annealing temperature of 140 °C. Surface carbon concentration of the SAM covered substrate increases (XPS C/Si atomic ratio increases from 3.5 to 5.4) and SAM structure moves from a largely disordered state to an ordered film with molecules tilted at $\sim 30^\circ$ versus the surface normal for the alkyl chains and the phenyl rings (NEXAFS) after annealing at 140 °C. Dielectric properties corroborate spectroscopic/AFM measurements as leakage current drops from 10^{-5} to 7.7×10^{-8} A cm^{-2} at 3 V. Pentacene OTFT performance is demonstrated on this low-voltage platform with operating voltages of less than 2 V, and mobility of up to $1.1 \text{ cm}^2 \text{ V}^{-1} \text{ s}^{-1}$.

Acknowledgments

This work is supported by the NSF-STC program under DMR-0120967, the AFOSR program under FA9550-09-1-0426. A. K. Y. Jen thanks the World Class University (WCU) program through the National Research Foundation of Korea under the Ministry of Education, Science and Technology (R31-10035). Part of this work was conducted at the University of Washington NanoTech User Facility, a member of the NSF National Nanotechnology Infrastructure Network (NNIN). The XPS experiments were done at the National ESCA and Surface Analysis Center for Biomedical Problems, which is supported by NIH grant EB-002027. The NEXAFS experiments were performed at the NSLS, Brookhaven National Laboratory, which is supported by the U.S. Department of Energy, Division of Materials Science and Division of Chemical Sciences

References

1. Sekitani T, Zschieschang U, Klauk H, Someya T. *Nat. Mater.* 2010; 9:1015–1022. [PubMed: 21057499]
2. Forrest SR. *Nature.* 2004; 428:911–918. [PubMed: 15118718]
3. Zaumseil J, Friend RH, Sirringhaus H. *Nat. Mater.* 2006; 5:69–74.
4. Muccini M. *Nat. Mater.* 2006; 5:605–613. [PubMed: 16880804]
5. Guo Y, Yu G, Liu Y. *Adv. Mater.* 2010; 22:4427–4447. [PubMed: 20853375]
6. Andringa A-M, Spijkman M-J, Smits ECP, Mathijssen SGJ, Hal PAV, Setayesh S, Willard NP, Borshchev OV, Ponomarenko SA, Blom PWM, de Leeuw DM. *Org. Electron.* 2010; 11:895–898.
7. Myny K, Steudel S, Smout S, Vicca P, Furthner F, van der Putten B, Tripathi AK, Gelinck GH, Genoe J, Dehaene W, Heremans P. *Org. Electron.* 2010; 11:1176–1179.
8. Lisong Z, Alfred W, Sheng-Chu W, Jie S, Sungkyu P, Thomas NJ. *Appl. Phys. Lett.* 2006; 88:083502.
9. Acton O, Osaka I, Ting G, Hutchins D, Ma H, McCullough R, Jen AK-Y. *Appl. Phys. Lett.* 2009; 95:113305.
10. Acton O, Dubey M, Weidner T, O'Malley KM, Kim T-W, Ting GG, Hutchins D, Baio JE, Lovejoy TC, Gage AH, Castner DG, Ma H, Jen AKY. *Adv. Funct. Mater.* 2010; 21:1476–1488.
11. Ma H, Yip H-L, Huang F, Jen AKY. *Adv. Funct. Mater.* 2010; 20:1371.
12. Horowitz G. *Adv. Mater.* 2010; 10:365–377.
13. DiBenedetto SA, Facchetti A, Ratner MA, Marks TJ. *Adv. Mater.* 2009; 21:1407–1433.
14. Ting GG, Acton O, Ma H, Ka JW, Jen AKY. *Langmuir.* 2009; 25:2140–2147. [PubMed: 19128035]
15. Michael N, Thomas S, Hendrik F, Marcus H. *Appl. Phys. Lett.* 2010; 98:093302.

16. Sekitani T, Yokota T, Zschieschang U, Klauk H, Bauer S, Takeuchi K, Takamiya M, Sakurai T, Someya T. *Science*. 2009; 326:1516–1519. [PubMed: 20007895]
17. Acton O, Hutchins D, Árnadóttir L, Weidner T, Cernetic N, Ting GG, Kim T-W, Castner DG, Ma H, Jen AKY. *Adv. Mater.* 2011; 23:1899–1902. [PubMed: 21438035]
18. Vuillaume D, Boulas C, Collet J, Davidovits JV, Rondelez F. *Appl. Phys. Lett.* 1996; 69:1646–1648.
19. Halik M, Klauk H, Zschieschang U, Schmid G, Dehm C, Schutz M, Maisch S, Effenberger F, Brunnbauer M, Stellacci F. *Nature*. 2004; 431:963–966. [PubMed: 15496917]
20. Maria AR, Olivier JAS, George MW. *Appl. Phys. Lett.* 1998; 72:1781–1783.
21. Kenjiro F, Takanori H, Tomoyuki Y, Tsuyoshi S, Ute Z, Hagen K, Takao S. *Appl. Phys. Lett.* 2009; 95:203301.
22. Yeong Don P, Do Hwan K, Yunseok J, Minkyu H, Jung Ah L, Kilwon C. *Appl. Phys. Lett.* 2005; 87:243509.
23. DiBenedetto SA, Frattarelli D, Ratner MA, Facchetti A, Marks TJ. *J. Am. Chem. Soc.* 2008; 130:7528–7529. [PubMed: 18498159]
24. Savard S, Blanchard LP, Léonard J, Prud'homme RE. *Poly. Compos.* 1984; 5:242–249.
25. Wang M, Liechti KM, Wang Q, White JM. *Langmuir*. 2005; 21:1848–1857. [PubMed: 15723481]
26. Kessel CR, Granick S. *Langmuir*. 1991; 7:532–538.
27. Samant MG, Brown CA, Gordon JG. *Langmuir*. 1993; 9:1082–1085.
28. Tao Y-T. *J. Am. Chem. Soc.* 1993; 115:4350–4358.
29. Allara DL, Nuzzo RG. *Langmuir*. 1985; 1:45–52.
30. Allara DL, Nuzzo RG. *Langmuir*. 1985; 1:52–66.
31. Allara DL, Atre SV, Ellinger CA, Snyder RG. *J. Am. Chem. Soc.* 1991; 113:1852–1854.
32. Smith EL, Porter MD. *J. Phys. Chem.* 1993; 97:8032–8038.
33. Chen SH, Frank CW. *Langmuir*. 1989; 5:978–987.
34. a) Dubey M, Weidner T, Gamble LJ, Castner DG. *Langmuir*. 2010; 26:14747–14754. [PubMed: 20735054] b) Zschieschang U, Halik M, Klauk H. *Langmuir*. 2008; 24:1665–1669. [PubMed: 18198917]
35. Thissen P, Valtiner M, Grundmeier G. *Langmuir*. 2009; 26:156–164. [PubMed: 20000361]
36. (a) Randon J, Blanc P, Paterson RJ. *Membr. Sci.* 1995; 98:119–129. (b) Hutchins DO, Acton O, Weidner T, Cernetic N, Baio JE, Ting G, Castner DG, Ma H, Jen AKY. *Org. Electron.* 2012; 13:464–468.
37. a) James MB, Paul HW, Florian C, Martin H, John EA, Iain M, Donal DCB, Thomas DA. *Appl. Phys. Lett.* 2009; 95:103310. b) Visscher I, Stuart MCA, Engberts JBF. *N. Org. Biomol. Chem.* 2006; 4:707–712.
38. Aswal DK, Lenfant S, Guerin D, Yakhmi JV, Vuillaume D. *Small*. 2005; 1:725–729. [PubMed: 17193515]
39. Acton O, Ting GG II, Ma H, Hutchins D, Wang Y, Purushothaman B, Anthony JE, Jen AKY. *J. Mater. Chem.* 2009; 19:7929–7936.
40. Nie H-Y, Walzak MJ, McIntyre NS. *J. Phys. Chem. B.* 2006; 110:21101–21108. [PubMed: 17048932]
41. Stöhr, J. *NEXAFS Spectroscopy*. Vol. Vol. 25. Berlin: Springer-Verlag; 1992.
42. Weidner T, Shaporenko A, Ballav N, Ulman A, Zhamikov M. *J. Phys. Chem. C.* 2008; 112:1191.
43. Weidner T, Shaporenko A, Müller J, Holtig M, Terfort A, Zharnikov MJ. *Phys. Chem. C.* 2007; 111:11627.
44. Weidner T, Zharnikov M, Hossbach J, Castner DG, Siemeling U. *J. Phys. Chem. C.* 2010; 114:14975.
45. Zharnikov M, Grunze M. *J. Phys. Condens. Matter.* 2001; 13:11333.
46. Hitchcock AP, Fischer P, Gedanken A, Robin MB. *J. Phys. Chem.* 1987; 91:531–540.
47. Frey S, Stadler V, Heister K, Eck W, Zharnikov M, Grunze M, Zeysing B, Terfort A. *Langmuir*. 2001; 17:2408–2415.
48. Outka DA, Stöhr J, Rabe JP, Swalen JD. *J. Chem. Phys.* 1988; 88:4076.

49. Dubey M, Gouzman I, Bernasek SL, Schwartz J. *Langmuir*. 2006; 22:4649–4653. [PubMed: 16649777]
50. Laibinis PE, Whitesides GM. *J. Am. Chem. Soc.* 1992; 114:1990–1995.
51. Li Z, Chang S-C, Williams RS. *Langmuir*. 2003; 19:6744–6749.
52. McGuinness CL, Diehl GA, Blasini D, Smilgies DM, Zhu M, Samarth N, Weidner T, Ballav N, Zharnikov M, Allara DL. *ACS Nano*. 2010; 4:3447–3465. [PubMed: 20481546]

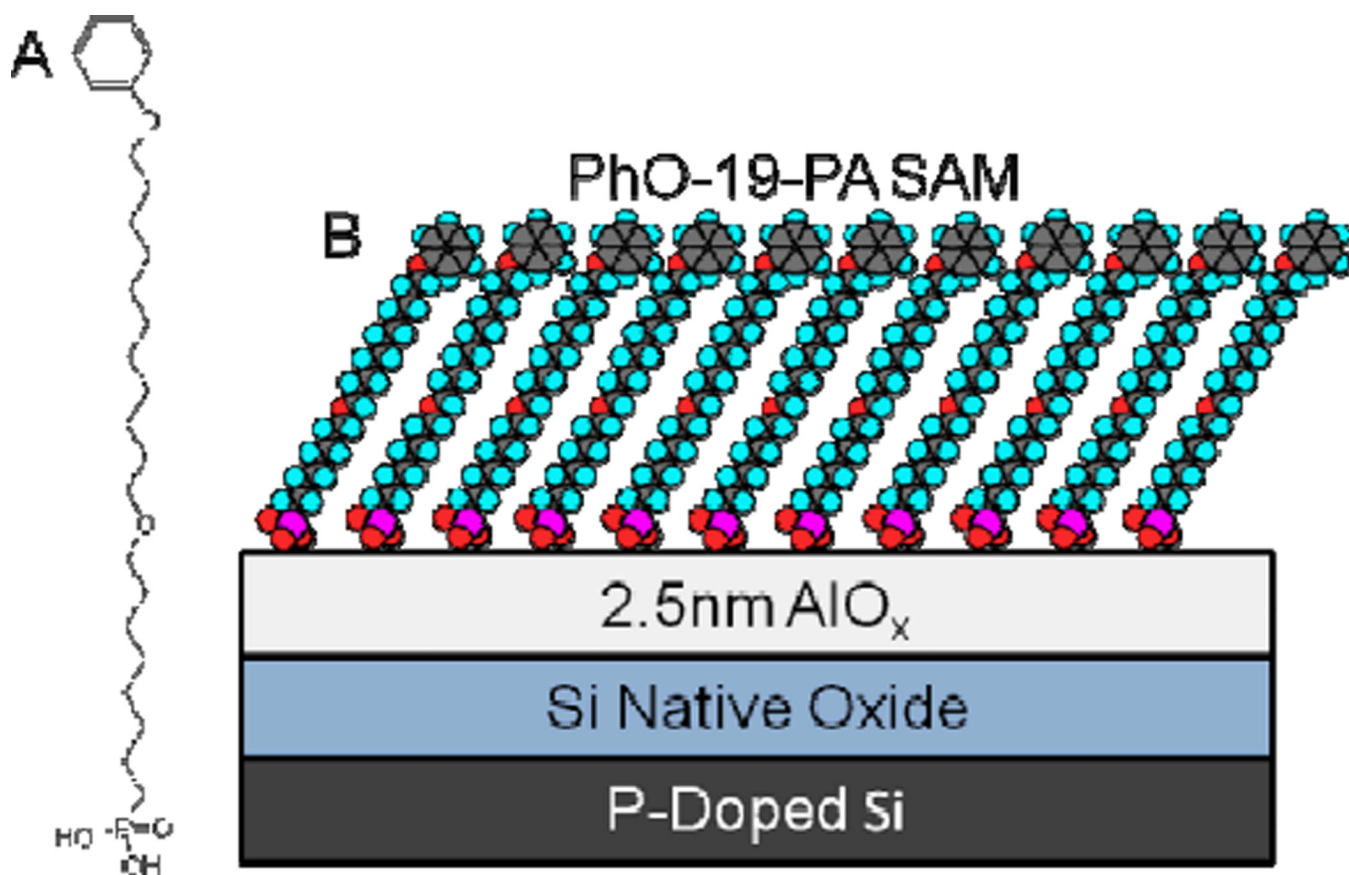


Figure 1. (A) Chemical structure of PhO-19-PA molecule. (B) Schematic of hybrid SAM-oxide dielectric used to study SAM densification through solid state annealing.

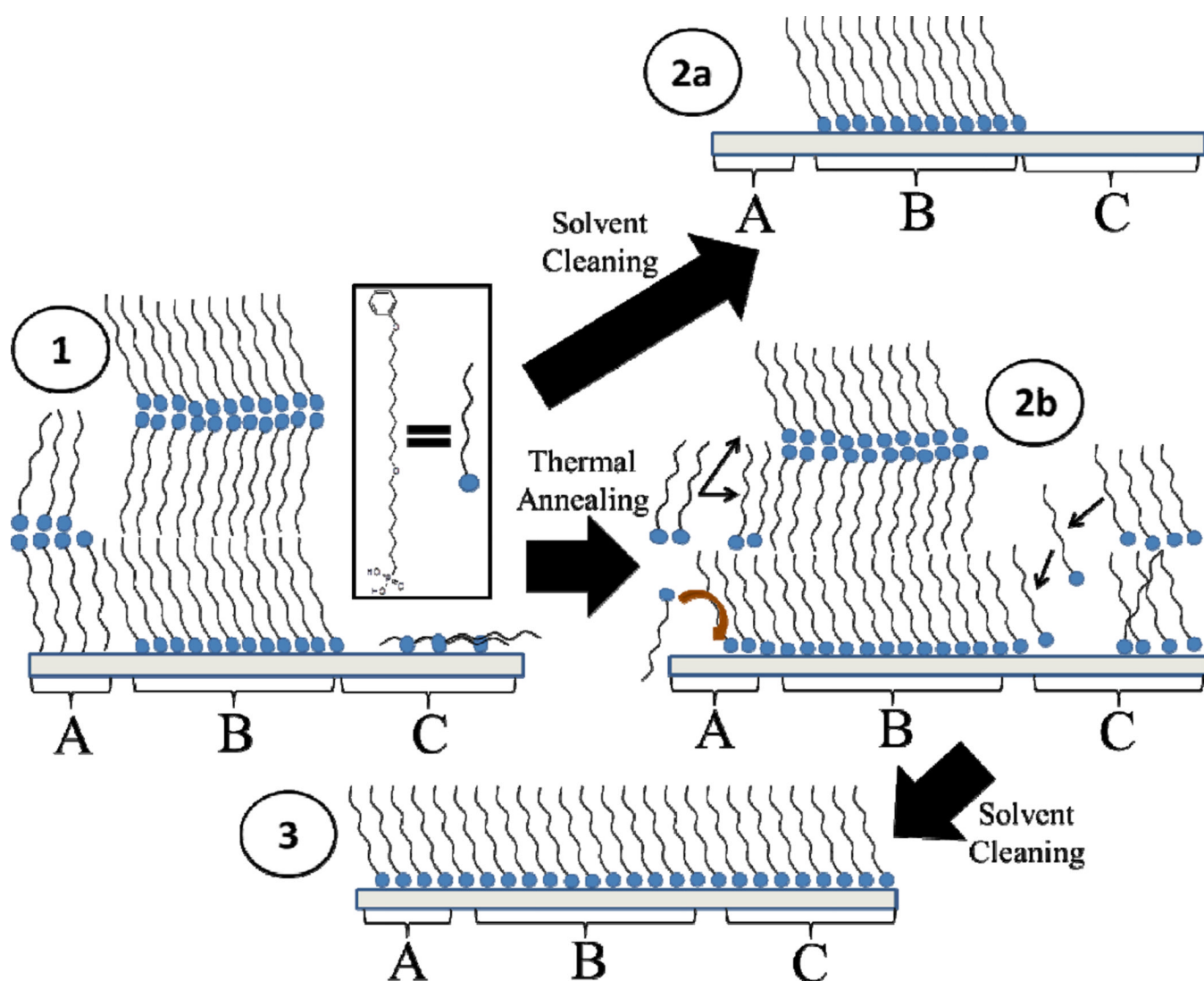


Figure 2. Illustration of proposed SAM densification mechanisms. Step 1: Spin coating of disordered as-cast multilayer film. A) PhO-19-PA molecules misoriented and unable to bind with surface. B) Multilayer formation with bound monolayer below. C) SAM lying flat on surface/voids in monolayer due to low density assembly. Step 2a: Multilayer removal prior to annealing, resulting in SAM island formation on substrate surface. A–C) Unbound/misoriented molecules are removed, with bound SAM islands remaining on the surface. Step 2b: Annealing of PhO-19-PA multilayer allowing SAM densification to occur. A) Reorientation of SAM molecules favorable to surface binding. B) Diffusion of SAM molecules across the substrate surface forming large droplets of residual PhO-19-PA material. C) Diffusion of PhO-19-PA across surface; filling in holes and “pushing up” low density structures. Step 3: Clean SAM after thermal annealing. A–C) Post cleaning a highly ordered, dense SAM is left on surface.

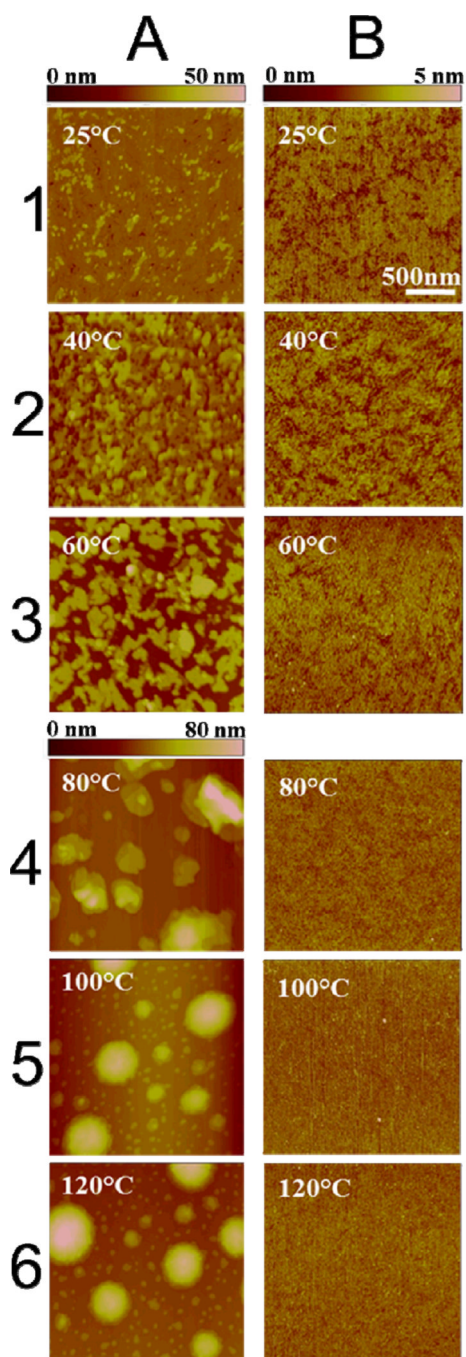


Figure 3. PhO-19-PA SAM densification through thermal annealing. (A) AFM images of as-cast PhO-19-PA multilayer film after annealing step. (B) AFM images of SAM surface after thermal annealing and solvent cleaning to remove bulk PhO-19-PA multilayer. Note: 500 nm horizontal scale bar applies to all images, vertical (colored) scale bars apply to images directly below scale bar.

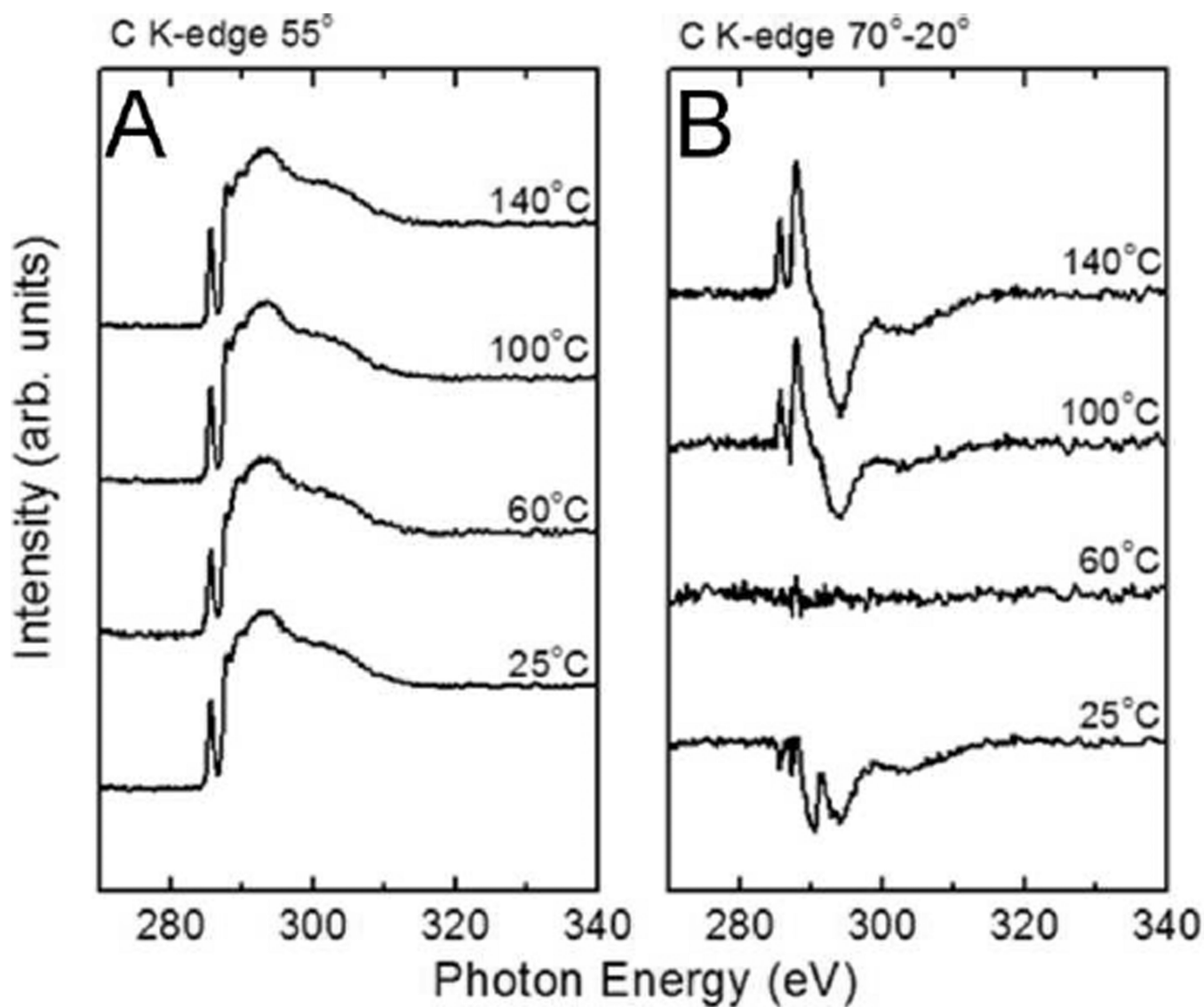


Figure 4. NEXAFS spectra of PhO-19-PA SAMs after spun cast bulk film is annealed at 25 °C, 60 °C, 100 °C, and 140 °C for 10 min., followed by solvent cleaning. (A) Carbon K-edge spectra acquired at a 55° incidence angle. (B) Carbon K-edge difference spectra (70°-20° angles).

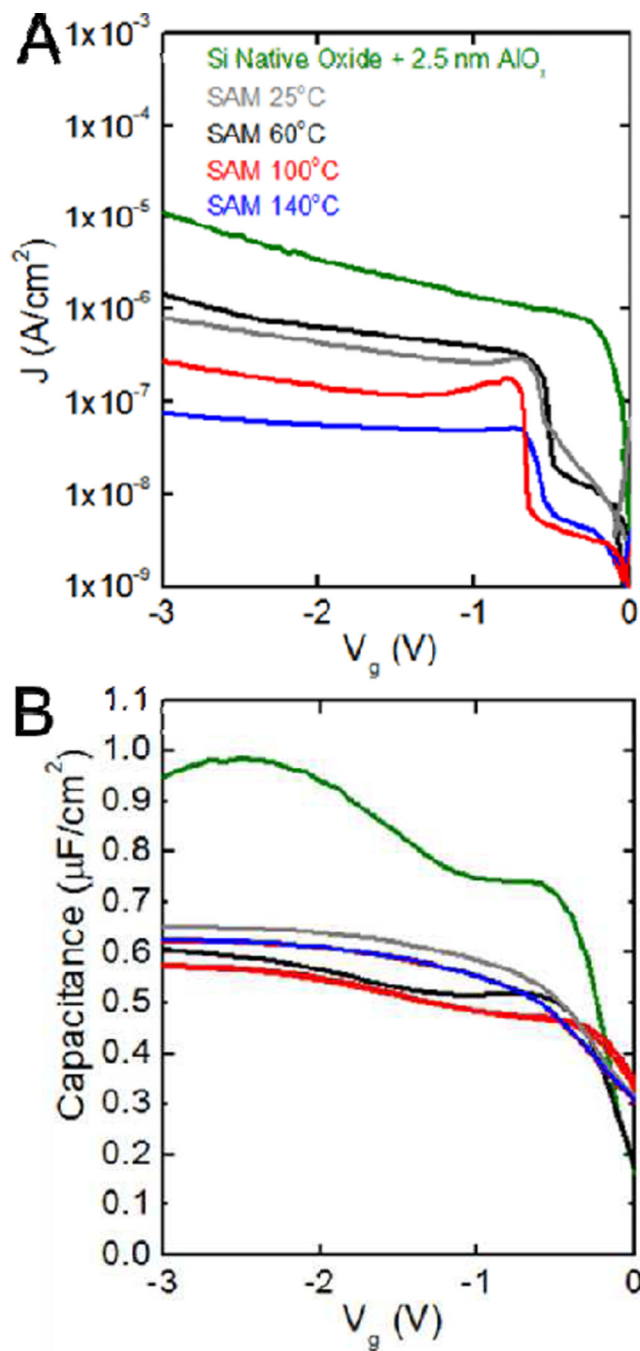


Figure 5.

(A) Plots of leakage current vs. voltage, and (B) capacitance vs. voltage for the metal-insulator-semiconductor (MIS) capacitor. Semiconductor: heavily doped P-type Si. Dielectric: SAM on 2.5 nm AlO_x and Si native oxide layers. Metal: 50 nm thermally evaporated Au. Bulk spun cast PhO-19-PA films were annealed at temperatures of 25 °C, 60 °C, 100 °C, 140 °C for 10 min, followed by solvent cleaning to form SAMs of increasing density and dielectric performance.

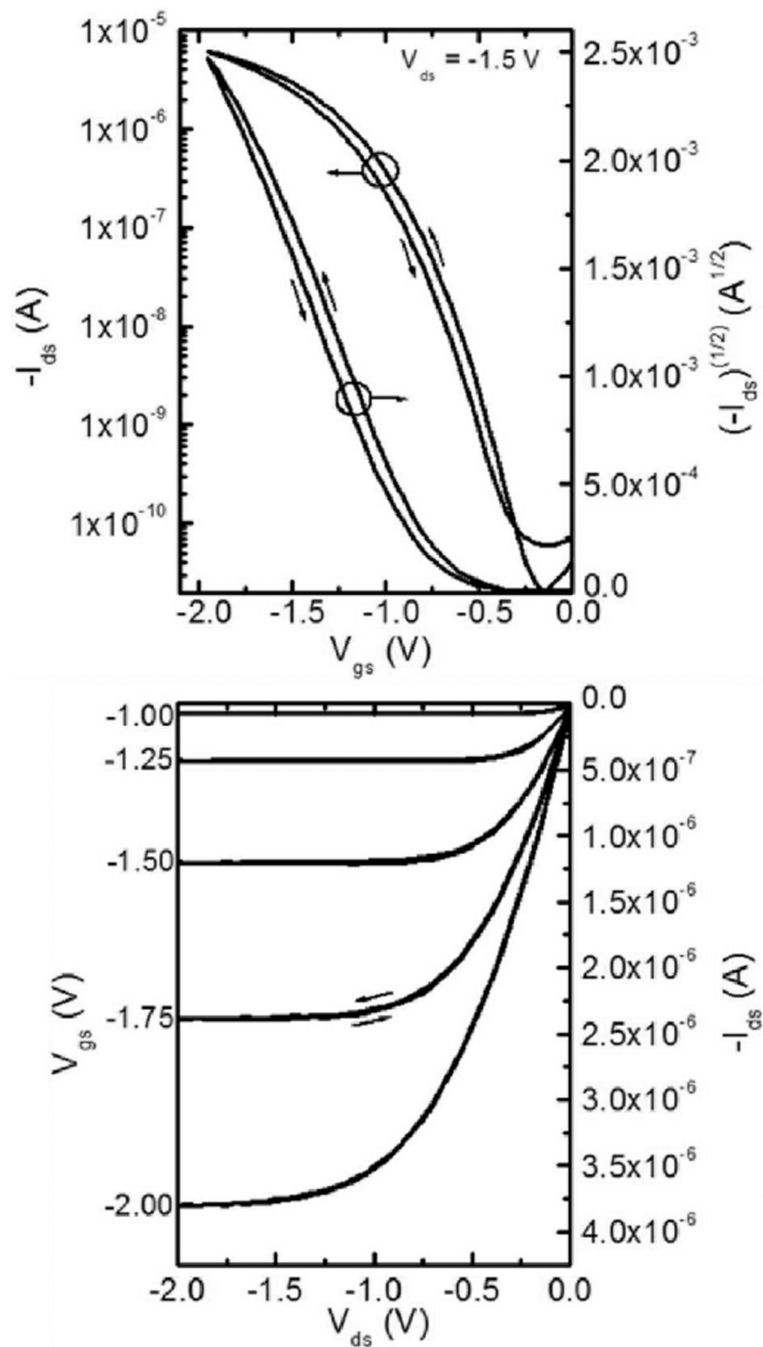
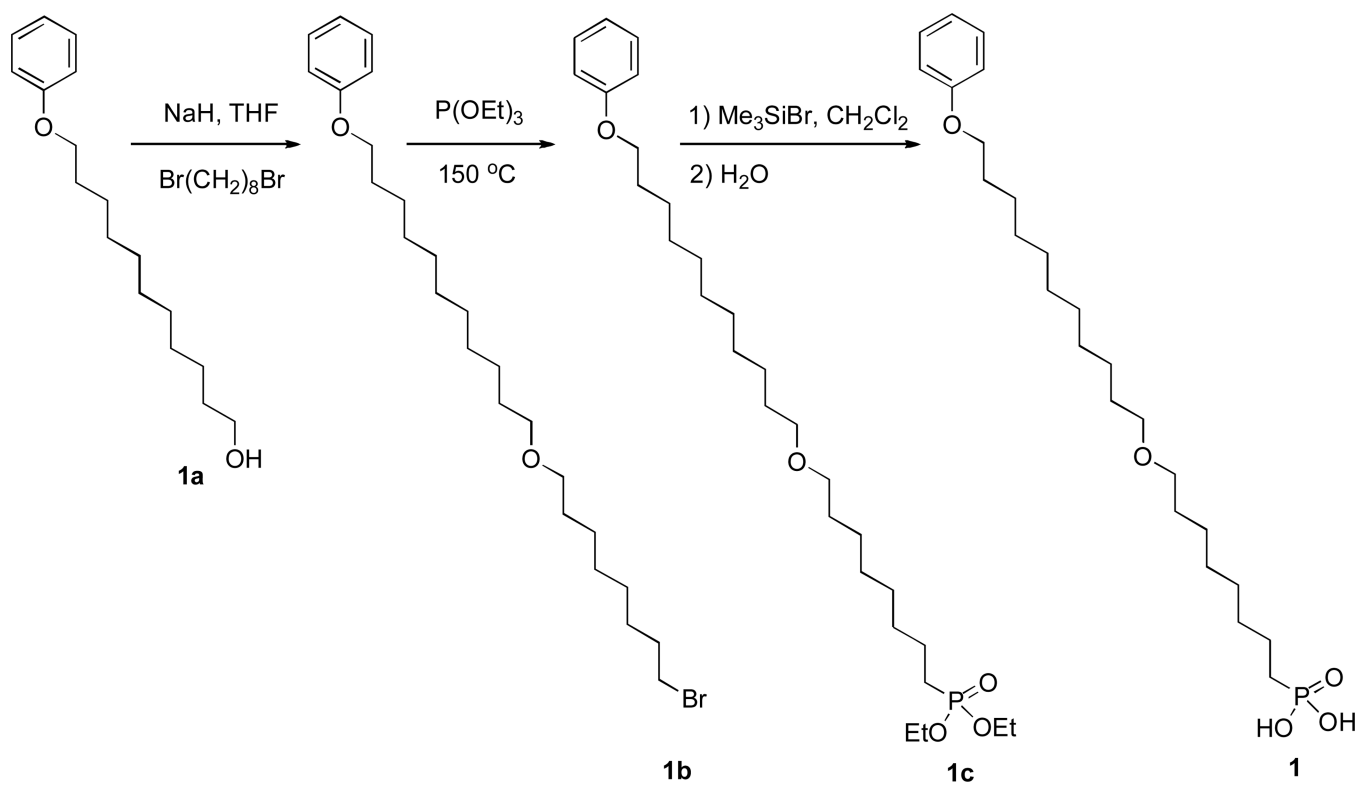


Figure 6. Characteristic transfer (A) and output curves (B) of top-contact pentacene FET devices made with an ultra-thin hybrid SAM-oxide dielectric ($W = 1000 \mu\text{m}$ $L = 20 \mu\text{m}$). PhO-19-PA SAM formed by spin casting, annealing at $140 \text{ }^\circ\text{C}$ for 10 min., and solvent cleaning.



Scheme 1.
Synthetic steps for the molecule of [8-(11-phenoxy-undecyloxy)-octyl]phosphonic acid (PhO-19-PA).

Table 1

XPS-derived atomic compositions for PhO-19-PA SAMs prepared by different annealing temperatures.

Temperature (°C)	C 1s	Si 2p	O 1s	P 2p	C/P	C/Si
25	54.0 (1.5)	15.6 (0.9)	28.7 (0.5)	1.8 (0.1)	30	3.5
60	57.2 (1.3)	15.8 (0.3)	24.9 (1.2)	2.2 (0.3)	26	3.6
100	62.4 (0.3)	12.7 (0.9)	23.0 (0.4)	2.0 (0.2)	32	4.9
140	62.9 (1.7)	11.6 (1.7)	23.5 (0.3)	2.0 (0.3)	32	5.4
Atomic % (stdv)						

Table 2

Summary of pentacene FET device performance utilizing hybrid SAM-oxide dielectric layer. Twenty devices from two batches were measured, all with $W = 1000 \mu\text{m}$ and $L = 20 \mu\text{m}$.

μ ($\text{cm}^2\text{V}^{-1}\text{s}^{-1}$) (High) Avg. \pm St.Dev.	V_t (V) Avg. \pm St.Dev.	S (mV/dec.) Avg. \pm St.Dev.	$I_{\text{on}}/I_{\text{off}}$ (Range)
(1.1) 0.67 ± 0.24	0.82 ± 0.12	126.6 ± 33.2	$1.1 \times 10^5 - 1.0 \times 10^6$